Electrical switching of magnetic order in an orbital Chern insulator

https://doi.org/10.1038/s41586-020-2963-8

Received: 16 April 2020

Accepted: 1 September 2020

Published online: 23 November 2020

Check for updates

H. Polshyn[1], J. Zhu[2], M. A. Kumar[1], Y. Zhang[1], F. Yang[1], C. L. Tschirhart[1], M. Serlin[1], K. Watanabe[3], T. Taniguchi[4], A. H. MacDonald[2] & A. F. Young[1]✉

Magnetism typically arises from the joint effect of Fermi statistics and repulsive Coulomb interactions, which favours ground states with non-zero electron spin. As a result, controlling spin magnetism with electric fields—a longstanding technological goal in spintronics and multiferroics[1,2]—can be achieved only indirectly. Here we experimentally demonstrate direct electric-field control of magnetic states in an orbital Chern insulator[3–6], a magnetic system in which non-trivial band topology favours long-range order of orbital angular momentum but the spins are thought to remain disordered[7–14]. We use van der Waals heterostructures consisting of a graphene monolayer rotationally faulted with respect to a Bernal-stacked bilayer to realize narrow and topologically non-trivial valley-projected moiré minibands[15–17]. At fillings of one and three electrons per moiré unit cell within these bands, we observe quantized anomalous Hall effects[18] with transverse resistance approximately equal to $h/2e^2$ (where h is Planck's constant and e is the charge on the electron), which is indicative of spontaneous polarization of the system into a single-valley-projected band with a Chern number equal to two. At a filling of three electrons per moiré unit cell, we find that the sign of the quantum anomalous Hall effect can be reversed via field-effect control of the chemical potential; moreover, this transition is hysteretic, which we use to demonstrate non-volatile electric-field-induced reversal of the magnetic state. A theoretical analysis[19] indicates that the effect arises from the topological edge states, which drive a change in sign of the magnetization and thus a reversal in the favoured magnetic state. Voltage control of magnetic states can be used to electrically pattern non-volatile magnetic-domain structures hosting chiral edge states, with applications ranging from reconfigurable microwave circuit elements to ultralow-power magnetic memories.

The quantized anomalous Hall effect[20] occurs in two-dimensional insulators whose filled bands have a finite net Chern number, and requires broken time-reversal symmetry. Chern bands arise naturally in graphene systems when the Dirac spectrum acquires a mass, for instance, owing to the breaking of sublattice symmetry in monolayer graphene by a hexagonal boron nitride (hBN) substrate[21]. In the absence of electron–electron interactions, bands located in the two inequivalent valleys at opposite corners of graphene's hexagonal Brillouin zone are constrained by time-reversal symmetry to acquire equal and opposite Chern numbers. In some graphene systems, a periodic moiré superlattice can be used to engineer superlattice bands that generically preserve the non-zero Chern numbers that arise from the incipient Berry curvature of the monolayer graphene Dirac points[22,23]. When the bandwidth of the superlattice bands is sufficiently small, the importance of electron–electron interactions is enhanced, leading to symmetry breaking that manifests primarily as resistivity peaks at integer filling of normally fourfold degenerate superlattice bands[24–26]. Among the states potentially favoured by electron–electron interactions are those with spontaneous breaking of time-reversal symmetry[8–14], and indeed ferromagnetism and quantum anomalous Hall effects have been observed in both twisted bilayer graphene (tBLG) aligned to hBN[3,4] and rhombohedral trilayer graphene, also aligned to hBN[5]. In contrast to quantum anomalous Hall effects observed in magnetically doped topological insulators, which are spin ferromagnets rendered strongly anisotropic by their large spin–orbit coupling, in graphene moiré systems, the spin–orbit coupling vanishes and the magnetism is thought to be primarily orbital, leading these systems to be dubbed 'orbital Chern insulators'.

Here we introduce another moiré heterostructure that shows quantum anomalous Hall effects. As shown in Fig. 1a, our devices consist of a graphene monolayer rotationally faulted with respect to Bernal-stacked graphene bilayer, which we refer to as twisted monolayer–bilayer graphene (tMBG). The tMBG moiré consists of a triangular lattice of ABB-stacked regions interspersed with more structurally stable ABA

[1]Department of Physics, University of California, Santa Barbara, Santa Barbara, CA, USA. [2]Department of Physics, University of Texas, Austin, TX, USA. [3]Research Center for Functional Materials, National Institute for Materials Science, Tsukuba, Japan. [4]International Center for Materials Nanoarchitectonics, National Institute for Materials Science, Tsukuba, Japan.
✉e-mail: andrea@physics.ucsb.edu

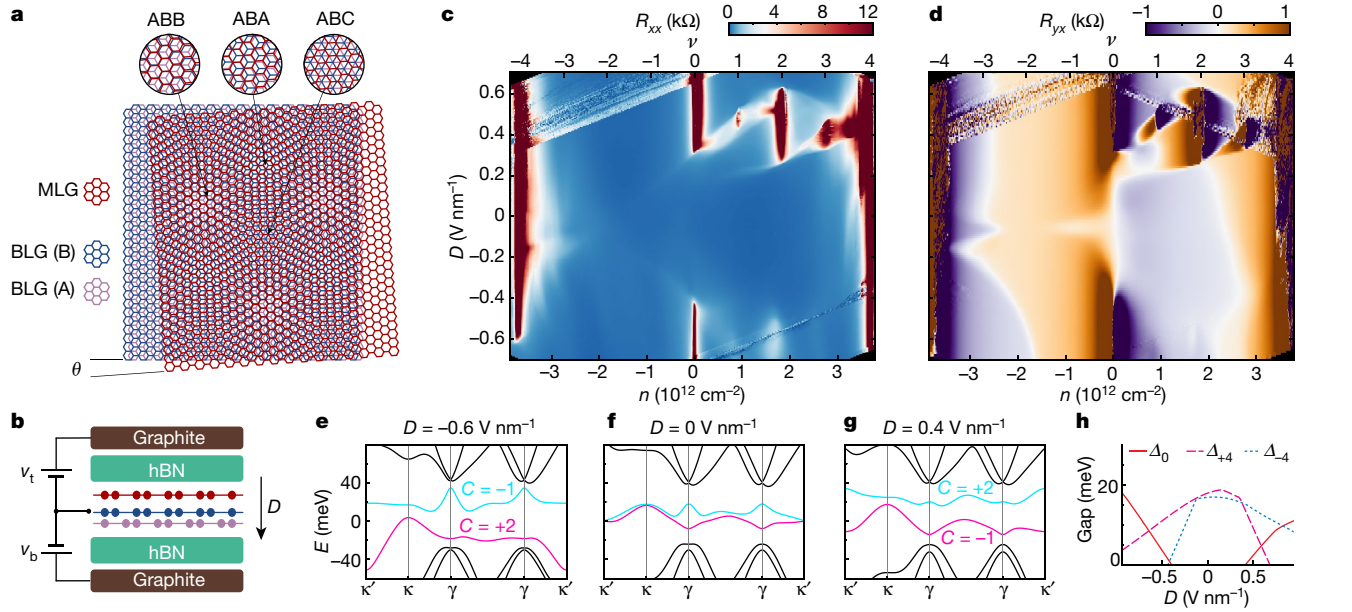

Fig. 1 | Twisted monolayer–bilayer graphene. a, Crystalline structure of small-angle tMBG. ABB regions form a triangular lattice separated by regions of ABA and ABC stacking. **b**, Schematic of our dual-gated devices. Top and bottom gate voltages v_t and v_b are used to control both total carrier density n and the electric displacement field D as described in the main text. **c**, **d**, Longitudinal resistance R_{xx} measured at $T = 1.35$ K (**c**) and transverse resistance R_{yx} measured at $T = 1.35$ K and $B = \pm 0.5$ T (**d**). Both are plotted as a function of carrier density n and D for device D1 with twist angle $\theta = 1.25°$. **e**, Band structure calculated from a continuum model (Methods, Supplementary Information) for $D = -0.6$ V nm^{-1}. **f**, **g**, Band structure for $D = 0$ V nm^{-1} (**f**) and $D = 0.4$ V nm^{-1} (**g**). **h**, Energy gaps (Δ_ν) calculated within the Hartree approximation (Supplementary Information) for $\nu = -4$, $\nu = 0$ and $\nu = +4$. In **e**–**h**, we use a dielectric constant $\varepsilon_{bg} = 4$ to convert the interlayer potential difference to a displacement field, $\Delta_U = eDd/\varepsilon_{bg}$, where $d = 3.3$ Å is the graphene interlayer separation.

and ABC regions, as illustrated in Fig. 1a; in the low-energy bands, wavefunctions are localized near the ABB regions. Our devices are fabricated by applying a 'cut-and-stack' method to an exfoliated graphene flake that contains both monolayer and bilayer graphene regions (Methods, Extended Data Fig. 1). Two graphite gates above and below the tMBG layer allow independent control of the overall carrier density $n = c_t v_t + c_b v_b$ and the electric displacement field $D = (c_t v_t - c_b v_b)/2\varepsilon_0$, where ε_0 is the vacuum permittivity, $v_{t(b)}$ is the applied voltage and $c_{t(b)}$ is the capacitance per unit area of the top (bottom) gate (Fig. 1b).

D-field tunable flat bands

Figure 1c, d shows the longitudinal and Hall resistance as a function of n and D for a device with interlayer twist angle $\theta \approx 1.25°$. Additional data from devices with a range of twist angles between 0.9° and 1.4° are shown in Extended Data Fig. 2. All devices show resistance peaks at $\nu = \pm 4$, where $\nu = nA_{u.c.}$ denotes the number of carriers per superlattice unit cell, $A_{u.c.} \approx \sqrt{3}a^2/(2\sin^2\theta)$ is the unit cell area and $a = 2.46$ Å is the lattice constant of graphene. Correlated states, revealed by sign changes in the Hall resistance and peaks in the longitudinal resistance, are observed near $\nu = 1$, $\nu = 2$ and $\nu = 3$ for devices with $\theta = 1.25°$ and $\theta = 1.4°$. They appear only within a narrow range of displacement fields near $D \approx 0.4$ V nm^{-1}, with onset temperatures as high as 20 K (Extended Data Fig. 3). In all such devices, an anomalous Hall effect is observed at $\nu = 1$ and $\nu = 3$, as shown in Extended Data Figs. 4, 5.

Similar observations in rotationally faulted bilayer–bilayer graphene[27–31] have been interpreted as arising from D-field-tuned formation of an isolated narrow band, and consequent spontaneous breaking of spin, valley or lattice symmetries that result in correlated insulating states at integer fillings. A previous theoretical study[15] has suggested that tMBG similarly hosts narrow electronic bands at small twist angles around 1.2°. In our data, the domains of the D field over which correlated physics is observed align with where numerical simulations (Fig. 1e–h) show the formation of a narrow, isolated band. The electronic band structure of tMBG arises from the moiré-induced hybridization of the monolayer graphene Dirac cone (located at the κ point in the band structure diagrams of Fig. 1e–g) with the parabolic low-energy band of the bilayer (at the κ′ point). When $D = 0$, low-energy valence and conduction bands are isolated from the other bands but overlap with each other, giving rise to gaps at $\nu = \pm 4$ but not at $\nu = 0$. At intermediate values of $|D|$, a gap opens at charge neutrality, leading to the formation of isolated conduction and valence bands with non-zero Chern number. Further increase of $|D|$ then leads to band overlap between the low-energy bands and higher-energy dispersive bands. Correlated states at integer filling, accompanied by 'halos' of changed resistance relative to the background at non-integer filling, appear in the intermediate regime where both calculations (Fig. 1h) and experimental data indicate the formation of a narrow and isolated conduction band.

Quantum anomalous Hall states with $C = 2$

We focus on the $n > 0$, $D > 0$ narrow-band regime, a detail of which is shown in Fig. 2a. At $\nu = 2$, we observe a robust insulator, consistent with a topologically trivial gap. At both $\nu = 1$ and $\nu = 3$, however, the resistance at magnetic field $B = 0$ is both noisy and comparatively low. Magnetoresistance measurements (Fig. 2b, c) reveal that the noise is due to magnetic hysteresis. In both cases, we observe rapid switching between states with transverse resistance $R_{yx} \approx \pm h/2e^2$ (where h is Planck's constant and e is the charge on the electron), accompanied by a low longitudinal resistance $R_{xx} \lesssim 1$ kΩ. The saturation of the Hall resistance near $h/2e^2$ is suggestive of polarization into bands with Chern number $C = 2$. The quantization is not precise, reaching only 85% of the expected value at $\nu = 3$, for instance. However, the evolution of the Hall plateau in the magnetic field, shown in Fig. 2d, e, provides further evidence of an underlying orbital Chern insulator state. For both $\nu = 1$ and $\nu = 3$, increasing the magnetic field shifts the centre of the plateau in density (n^*), in agreement with the Středa formula[32], $C = (h/e)(\partial n^*/\partial B)$, which is applicable to any incompressible Chern insulator. Bands with $C = 2$ were previously predicted[15] and are consistent with our own band

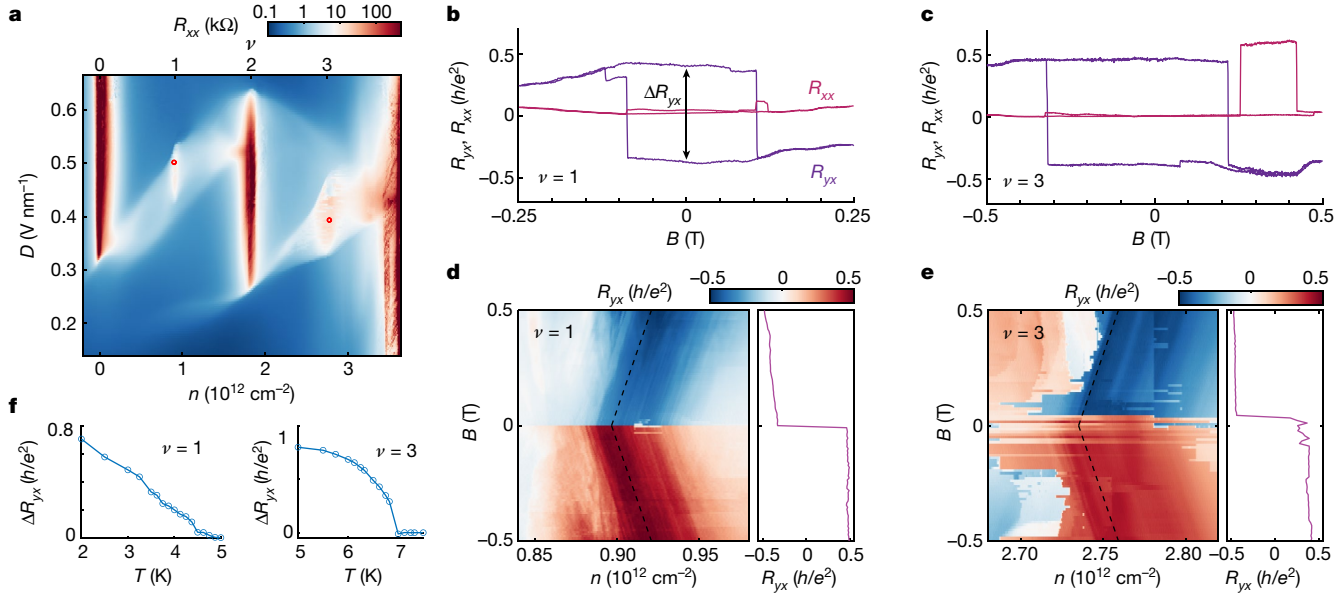

Fig. 2 | Orbital Chern insulators with $C = 2$. a, High-resolution plot of R_{xx} measured at $T = 1.35$ K and $B = 0$ T in device D1. **b**, **c**, R_{yx} and R_{xx} measured as a function of B at 1.43 K near $\nu = 1$, at $n = 0.9 \times 10^{12}$ cm^{-2} and $D = 0.5$ V nm^{-1} (**b**) and near $\nu = 3$, at $n = 2.77 \times 10^{12}$ cm^{-2} and $D = 0.39$ V nm^{-1} (**c**). **d**, **e**, B and n dependence of R_{yx} near $\nu = 1$ measured at $T = 20$ mK (**d**) and near $\nu = 3$ measured at $T = 1.35$ K (**e**). In these measurements, the fast sweep axis is n. Dashed lines show the slope expected for gaps associated with $C = 2$, matching the n–B evolution of the plateaus in R_{yx}. Right insets in **d** and **e** show R_{yx} plotted along the dashed lines. **f**, Temperature dependence of the hysteresis loop height at $B = 0$ T, ΔR_{yx} for $\nu = 1$ and $\nu = 3$. Hysteresis vanishes at $T_C \approx 5$ K and $T_C \approx 7$ K, respectively, defining a lower bound for the Curie temperature.

structure calculation, which indicated that the conduction band has $C = 2$ for a positive D field.

It is notable that tMBG, in contrast to both rhombohedral trilayer graphene and tBLG, does not rely on precise alignment to hBN, making it an all-carbon quantum anomalous Hall system. However, our observations at $\nu = 1$ and $\nu = 3$ are in many ways qualitatively similar to the quantum anomalous Hall effect characterizations reported previously[3–5]. For instance, the magnetic transitions tend to occur via several discrete steps, corresponding to a small number of micrometre-size mesoscopic domain reversals. Temperature-dependent measurements show Curie temperatures—defined here by the onset of hysteresis—of $T_C \approx 5$ K for $\nu = 1$ and $T_C \approx 7$ K for $\nu = 3$ (see Fig. 2f as well as Extended Data Figs. 6, 7), again similar to previous reports of ferromagnetism in moiré heterostructures[3–5]. We expect the lack of perfect quantization to arise from a disorder-induced domain structure, as recently observed for similar states in tBLG[33].

Magnetization reversal

Striking new phenomena are, however, observed in the n-dependence of the Hall effect. Specifically, although R_{yx} changes smoothly as a function of n near the $\nu = 1$ orbital Chern insulator, it shows erratic switching behaviour near $\nu = 3$ (Fig. 2d, e). To investigate this phenomenon, we perform a dense series of hysteresis loop measurements in the vicinity of $\nu = 3$ at higher temperature, where we expect that domain wall pinning is weaker and hysteretic effects are somewhat suppressed. Although the sign of the anomalous Hall resistance is constant near $\nu = 1$, it reverses abruptly on crossing $\nu = 3$ (Fig. 3a–c). The sign reversal occurs with minimal change in the magnitude of R_{yx}, which remains close to the quantized value. This suggests that the reversal occurs via a change in the product of the magnetization sign and the Chern number sign, which we refer to as the magnetic state. This is further evidenced by the n–B map of R_{yx} (Fig. 3d), which shows that the R_{yx} changes sign at $n \approx 2.76 \times 10^{12}$ cm^{-2}, corresponding to $\nu = 3$. An additional manifestation of the inversion of the sign of the magnetization of a given magnetic state is the abrupt upturn in the coercive field in the close vicinity of the reversal point shown in Fig. 3b. This phenomenon is qualitatively consistent with a picture in which the total magnetization M changes sign for a fixed sense of valley polarization by passing through zero; near $M = 0$, the coupling to the magnetic field vanishes, leading to a divergence of the coercive field.

We propose that the magnetization reversal arises from the unique features of orbital Chern insulators. In particular, the protected edge states required by their non-trivial topology are occupied and contribute to the magnetization when the insulator is slightly n-doped, but not when it is slightly p-doped[19]. The edge-state contribution leads to a jump δM in the magnetization across the Chern insulator gap

$$\delta M = C \frac{\Delta}{\pi\hbar^2/m_e A_{\mathrm{u.c.}}} \frac{\mu_B}{A_{\mathrm{u.c.}}} \quad (1)$$

where $\hbar$ is the reduced Planck's constant, m_e is the electron mass, $A_{\mathrm{u.c.}}$ is the unit cell area, Δ is the gap and μ_B is the Bohr magneton. Although this effect is present in all Chern insulators, it is negligible in magnetically doped topological insulators[18] where time-reversal symmetry is broken primarily by spontaneous spin polarization. In these systems, the total spin magnetization is of the order of $1\,\mu_B/A_{\mathrm{u.c.}}$. As Δ is on the order of a few millielectronvolts, $\Delta \ll \hbar^2/(m_e A_{\mathrm{u.c.}})$ and the edge-state orbital magnetization is dwarfed by spin magnetization. In graphene moiré orbital Chern insulators, the bulk orbital magnetization is again of the order of $1\mu_B/A_{\mathrm{u.c.}}$ (refs. [19,33]). However, the large unit cell area allows for the prefactor in equation (1) to be of comparable or larger magnitude. When this edge-state contribution is sufficiently large, it can lead to a reversal in the sign of the net magnetization across the energy gap. For instance, taking measured energy gaps for quantum anomalous Hall states in tBLG[4] produces an estimate of $\delta M \approx \mu_B/A_{\mathrm{u.c.}}$. Indeed, a re-examination of transport data from the tBLG device aligned to hBN studied in ref. [4] finds a similar, though much less dramatic, change in the sense of the hysteresis loop accompanied by a similar divergence of the coercive field near (though not precisely at) $\nu = 3$ (Extended Data Fig. 8). We note that the magnetization of an orbital magnet can in principle change sign at any filling factor, but that it is more likely at integer ν because the

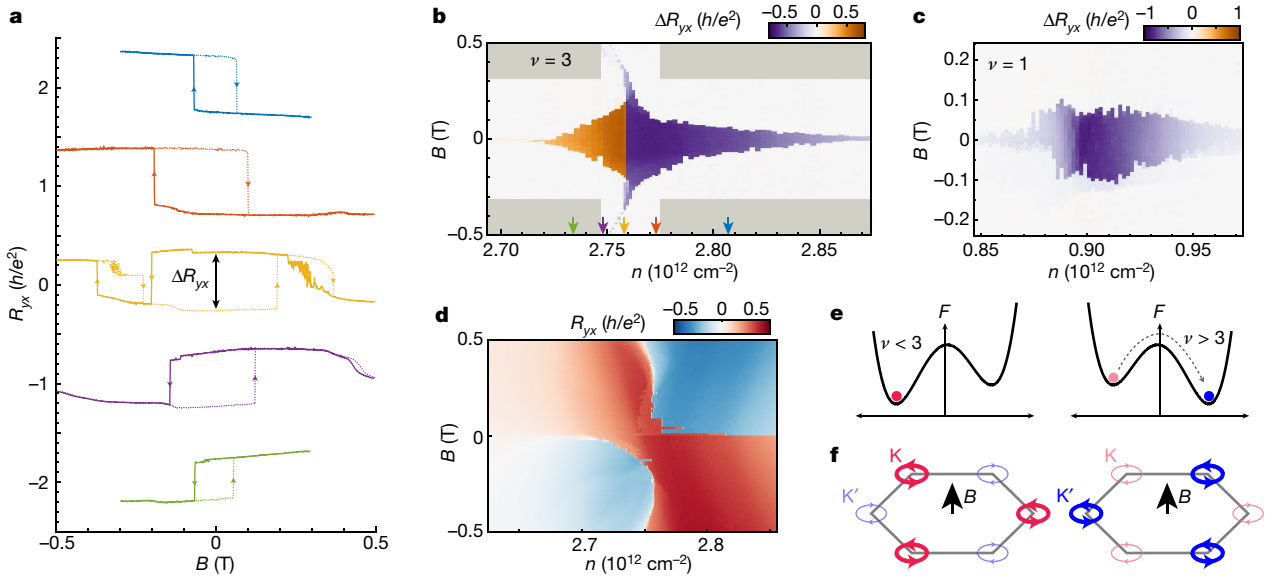

Fig. 3 | Doping induced magnetization reversal. a, Hysteresis loops measured at $T = 6.4$ K for several densities near $\nu = 3$. From top to bottom, $n = 2.807 \times 10^{12}$, 2.773×10^{12}, 2.758×10^{12}, 2.748×10^{12} and 2.734×10^{12} cm^{-2}, with colours corresponding to arrows in **b**. Curves are offset by h/e^2. **b**, $\Delta R_{yx} = R_{yx}^{B\downarrow} - R_{yx}^{B\uparrow}$ near $\nu = 3$ measured at 6.4 K. **c**, ΔR_{yx} near $\nu = 1$ measured at $T \approx 20$ mK. **d**, R_{yx} as a function of field and doping at 6.4 K with doping the fast sweep direction. **e**, Schematic of the free energy F versus order parameter for the two magnetic states. For a fixed sense of valley polarization, the orbital magnetization reverses sign with doping. **f**, At a fixed magnetic field, the system therefore switches between K and K′ valley polarization.

magnetization is discontinuous at this density. The conditions under which the reversal occurs are discussed in Methods.

Electrical switching of magnetic states

As an external magnetic field favours the state with magnetization aligned with the field, changing the sign of M is predicted to drive a reversal of the valley polarization as the chemical potential crosses the gap (Fig. 3e, f). The quantized Hall effect sign reversal is thus due to a change in magnetic state, in contrast to previously observed anomalous Hall effect sign reversals[34,35] arising from a change in the sign of the total anomalous Hall effect for a given magnetic state. As a result, electric-field-induced hysteretic behaviour is possible in our case as the two states are separated by an energy barrier. Figure 4a depicts the difference (again denoted ΔR_{yx}) between traces and retraces of field-effect-tuned density, acquired as B is stepped. Near $\nu = 3$, R_{yx} shows a finite signal in this channel, indicating hysteresis in gate voltage sweeps at fixed magnetic fields as high as several hundred millitesla.

Electric-field control of magnetic states provides a reliable experimental 'knob' to realize non-volatile switching of magnetization. We find that at $B = 80$ mT, $n = 2.77 \times 10^{12}$ cm^{-2} and $T = 6.4$ K, states of opposite polarization can be controllably switched using excursions in either n or B, as shown in Fig. 4b. Figure 4c shows this principle applied to non-volatile switching of the magnetic state using both B excursions at constant n and n excursions at constant B. Switches occur with perfect fidelity and appear to be indefinitely non-volatile at this temperature. We note that as for current- and magnetic-field-driven switching, the excellent reproducibility of field-effect switching ultimately arises from the absence of states with partial or intermediate valley polarization, or, equivalently, the extreme anisotropy inherent in a purely orbital two-dimensional magnet.

Orbital magnets realized at room temperature would be immediately applicable as embedded magnetic memory in logic devices. Candidates for higher-temperature operation include other moiré systems in which the lattice constant is smaller and the correlation energy consequently larger, assembled either by van der Waals stacking or using non-epitaxial growth techniques[36]. Even when restricted to cryogenic temperatures, there are several immediate opportunities that leverage gate-switchable chirality in a quantum anomalous Hall system. As a simple example, orbital Chern insulators could be used as the central elements in reconfigurable and compact microwave circulators[37], which may be useful for scaling up quantum information processing.

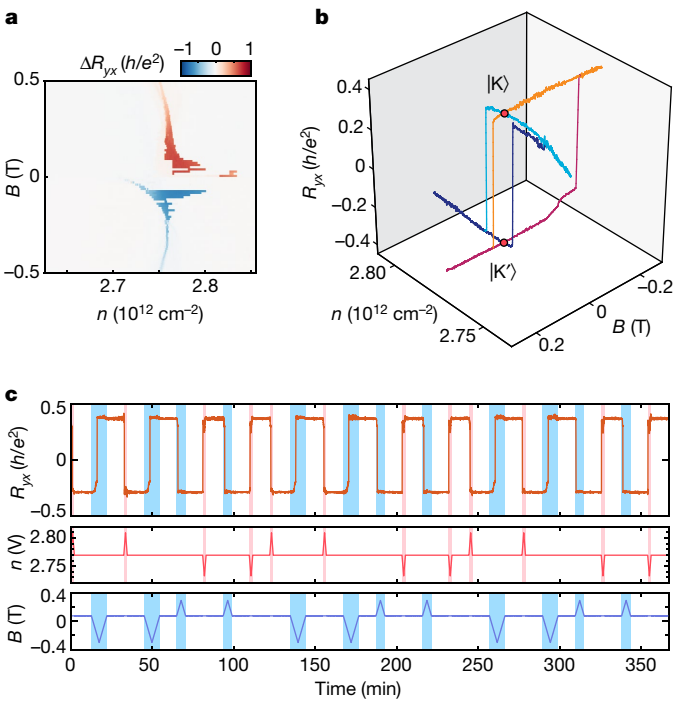

Fig. 4 | Non-volatile electrical control of a magnetic state at $T = 6.4$ K. **a**, Electric-field hysteresis. The colour scale encodes the difference between trace and retrace as the density is swept using electrostatic gates, with each trace–retrace taken at a fixed magnetic field. The reproducibility of magnetization switches is shown in Extended Data Fig. 9. **b**, Examples of hysteresis loops in both n and B. **c**, Time series of alternating pulses of field-effect density and magnetic field showing reproducible and non-volatile switching of the magnetic state, as read by the resulting Hall resistance.

Meanwhile, integrating orbital Chern insulators with superconductors may permit new device architectures devoted to the detection and manipulation of extended Majorana zero modes[38]. Our results highlight the novel opportunities for controlling functionality that arise from the realization of purely orbital magnetic systems.

Online content

Any methods, additional references, Nature Research reporting summaries, source data, extended data, supplementary information, acknowledgements, peer review information; details of author contributions and competing interests; and statements of data and code availability are available at https://doi.org/10.1038/s41586-020-2963-8.

1. Matsukura, F., Tokura, Y. & Ohno, H. Control of magnetism by electric fields. *Nat. Nanotechnol.* **10**, 209–220 (2015).
2. Jiang, S., Shan, J. & Mak, K. F. Electric-field switching of two-dimensional van der Waals magnets. *Nat. Mater.* **17**, 406–410 (2018).
3. Sharpe, A. L. et al. Emergent ferromagnetism near three-quarters filling in twisted bilayer graphene. *Science* **365**, 605–608 (2019).
4. Serlin, M. et al. Intrinsic quantized anomalous Hall effect in a moiré heterostructure. *Science* **367**, 900–903 (2020).
5. Chen, G. et al. Tunable correlated Chern insulator and ferromagnetism in a moiré superlattice. *Nature* **579**, 56–61 (2020); correction **581**, E3 (2020).
6. Lu, X. et al. Superconductors, orbital magnets and correlated states in magic-angle bilayer graphene. *Nature* **574**, 653–657 (2019).
7. Xie, M. & MacDonald, A. Nature of the correlated insulator states in twisted bilayer graphene. *Phys. Rev. Lett.* **124**, 097601 (2020).
8. Bultinck, N., Chatterjee, S. & Zaletel, M. P. Mechanism for anomalous Hall ferromagnetism in twisted bilayer graphene. *Phys. Rev. Lett.* **124**, 166601 (2020).
9. Zhang, Y.-H., Mao, D. & Senthil, T. Twisted bilayer graphene aligned with hexagonal boron nitride: anomalous Hall effect and a lattice model. *Phys. Rev. Res.* **1**, 033126 (2019).
10. Liu, J. & Dai, X. Theories for the correlated insulating states and quantum anomalous Hall phenomena in twisted bilayer graphene. Preprint at https://arxiv.org/abs/1911.03760 (2020).
11. Wu, F. & Das Sarma, S. Collective excitations of quantum anomalous Hall ferromagnets in twisted bilayer graphene. *Phys. Rev. Lett.* **124**, 046403 (2020).
12. Chatterjee, S., Bultinck, N. & Zaletel, M. P. Symmetry breaking and skyrmionic transport in twisted bilayer graphene. *Phys. Rev. B* **101**, 165141 (2020).
13. Repellin, C., Dong, Z., Zhang, Y.-H. & Senthil, T. Ferromagnetism in narrow bands of moiré superlattices. *Phys. Rev. Lett.* **124**, 187601 (2020).
14. Alavirad, Y. & Sau, J. D. Ferromagnetism and its stability from the one-magnon spectrum in twisted bilayer graphene. Preprint at https://arxiv.org/abs/1907.13633 (2019).
15. Ma, Z. et al. Topological flat bands in twisted trilayer graphene. Preprint at https://arxiv.org/abs/1905.00622 (2019).
16. Park, Y., Chittari, B. L. & Jung, J. Gate-tunable topological flat bands in twisted monolayer-bilayer graphene. *Phys. Rev. B* **102**, 035411 (2020).
17. Rademaker, L., Protopopov, I. V. & Abanin, D. A. Topological flat bands and correlated states in twisted monolayer-bilayer graphene. *Phys. Rev. Res.* **2**, 033150 (2020).
18. Chang, C.-Z. et al. Experimental observation of the quantum anomalous Hall effect in a magnetic topological insulator. *Science* **340**, 167–170 (2013).
19. Zhu, J., Su, J.-J. & MacDonald, A. H. The curious magnetic properties of orbital Chern insulators. Preprint at https://arxiv.org/abs/2001.05084 (2020).
20. Haldane, F. D. M. Model for a quantum Hall effect without Landau levels: condensed-matter realization of the "parity anomaly". *Phys. Rev. Lett.* **61**, 2015–2018 (1988).
21. Song, J. C. W., Samutpraphoot, P. & Levitov, L. S. Topological Bloch bands in graphene superlattices. *Proc. Natl Acad. Sci. USA* **112**, 10879–10883 (2015).
22. Zhang, Y.-H., Mao, D., Cao, Y., Jarillo-Herrero, P. & Senthil, T. Nearly flat Chern bands in moiré superlattices. *Phys. Rev. B* **99**, 075127 (2019).
23. Liu, J., Ma, Z., Gao, J. & Dai, X. Quantum valley Hall effect, orbital magnetism, and anomalous Hall effect in twisted multilayer graphene systems. *Phys. Rev. X* **9**, 031021 (2019).
24. Bistritzer, R. & MacDonald, A. H. Moiré bands in twisted double-layer graphene. *Proc. Natl Acad. Sci. USA* **108**, 12233–12237 (2011).
25. Cao, Y. et al. Correlated insulator behaviour at half-filling in magic-angle graphene superlattices. *Nature* **556**, 80–84 (2018).
26. Chen, G. et al. Evidence of a gate-tunable Mott insulator in a trilayer graphene moiré superlattice. *Nat. Phys.* **15**, 237–241 (2019).
27. Shen, C. et al. Correlated states in twisted double bilayer graphene. *Nat. Phys.* **16**, 520–525 (2020).
28. Liu, X. et al. Tunable spin-polarized correlated states in twisted double bilayer graphene. *Nature* **583**, 221–225 (2020).
29. Cao, Y. et al. Tunable correlated states and spin-polarized phases in twisted bilayer–bilayer graphene. *Nature* **583**, 215–220 (2020); correction **583**, E27 (2020).
30. Burg, G. W. et al. Correlated insulating states in twisted double bilayer graphene. *Phys. Rev. Lett.* **123**, 197702 (2019).
31. He, M. et al. Symmetry breaking in twisted double bilayer graphene. *Nat. Phys.* https://doi.org/10.1038/s41567-020-1030-6 (2020).
32. Streda, P. Quantised Hall effect in a two-dimensional periodic potential. *J. Phys. C* **15**, L1299 (1982).
33. Tschirhart, C. L. et al. Imaging orbital ferromagnetism in a moiré Chern insulator. Preprint at https://arxiv.org/abs/2006.08053 (2020).
34. Chiba, D. et al. Anomalous Hall effect in field-effect structures of (Ga,Mn)As. *Phys. Rev. Lett.* **104**, 106601 (2010).
35. Zhang, S. et al. Experimental observation of the gate-controlled reversal of the anomalous Hall effect in the intrinsic magnetic topological insulator $MnBi_2Te_4$ device. *Nano Lett.* **20**, 709–714 (2020).
36. Beekman, M., Heideman, C. L. & Johnson, D. C. Ferecrystals: non-epitaxial layered intergrowths. *Semicond. Sci. Technol.* **29**, 064012 (2014).
37. Viola, G. & DiVincenzo, D. P. Hall effect gyrators and circulators. *Phys. Rev. X* **4**, 021019 (2014).
38. Lian, B., Sun, X.-Q., Vaezi, A., Qi, X.-L. & Zhang, S.-C. Topological quantum computation based on chiral Majorana fermions. *Proc. Natl Acad. Sci. USA* **115**, 10938–10942 (2018).

Methods

Device fabrication

van der Waals heterostructures for tMBG devices were fabricated using a dry transfer technique based on a polycarbonate film on top of a polydimethyl siloxane (PDMS) stamp. The heterostructure was assembled in two steps to minimize the chance of disturbing the twist angle at the critical monolayer–bilayer interface. First, a two-layer stack with hBN at the top and a graphite layer at the bottom was picked up and transferred to a bare silicon/silicon dioxide wafer. This partial stack was annealed in vacuum at 400 °C to remove polymer residues from the top surface. A second stack consisting (from top to bottom) of hBN–FLG–hBN–MLG–BLG (where FLG, MLG and BLG are few-layer, monolayer and bilayer graphene, respectively) was then assembled and transferred on top of the first one. Crucially, the angle registry between the MLG and BLG was ensured by starting from a single exfoliated flake that includes both MLG and BLG domains. The flake was then cut with a conducting atomic force microscope tip in air (Extended Data Fig. 1). The MLG piece was picked up using a PDMS stamp and an interlayer twist introduced by substrate rotation. Then the BLG piece was picked up. All flakes except MLG and BLG were picked up at approximately 90 °C; the MLG, BLG and the transfer to the final substrate were carried out at 30 °C to preserve the twist angle of the structure. Devices were then fabricated using standard e-beam lithography and CHF_3/O_2 etching, and edge contacts were made by deposition of chromium/palladium/gold (1.5 nm/15 nm/250 nm).

Device characterization

Transport measurements were performed using SRS lock-in amplifiers, current preamplifiers (DL Instruments) and voltage preamplifiers (SRS) with typical excitations in the range 1–10 nA at 17.77 Hz. Measurements were performed in either a cryogen-free dilution refrigerator, with the sample in vacuum, or, in the case of Extended Data Fig. 3, in a wet variable-temperature insert with the sample in helium vapour.

For devices D1 and D2, the twist angle was determined from the position of the correlated insulating states. For devices D3 and D4, the twist angle was determined from the periodicity of the Hofstadter features observed in the magnetic field that arise from the interplay of the moiré superlattice period and magnetic length.

Band structure simulations

Band structure simulations were performed within a continuum model analogous to that of ref. [24] for the coupling between the top and middle layers, whereas the middle and bottom layers were treated as Bernal-stacked bilayer graphene. More details are in Supplementary Information.

Electrical reversibility

Why is the field-effect reversibility so robust in tMBG at $\nu = 3$, but weak in tBLG at $\nu = 3$ and absent at other filling factors in either system? Field reversibility requires that the edge-state contribution to the magnetization, δM, reverses the sign of the total magnetization. Our calculations for both tMBG and tBLG aligned to hBN indicate that δM and M_{bulk}—defined as the total magnetization when the chemical potential is at the bottom of the gap—normally have opposite sign. To ensure field reversibility, one thus wants to maximize the magnitude of the edge-state contribution while minimizing the magnitude of the bulk contribution. The large Chern numbers in tMBG are certainly helpful in this regard, as they increase δM. In addition, our theoretical analysis indicates that in odd-layer systems, exchange splitting between bands arising from valley polarization further decreases the magnitude of M_{bulk}. This effect, which includes contributions from bands far from the Fermi level, is present in tMBG but absent in tBLG (see Supplementary Information for details). The exchange contribution is expected to be larger at $\nu = 3$ than at $\nu = 1$, possibly explaining why we see reversible Chern insulators at $\nu = 3$ but conventional Chern insulators at $\nu = 1$ in tMBG.

Data availability

Source data are available for this paper. All other data that support the plots within this paper and other findings of this study are available from the corresponding author upon reasonable request. Source data are provided with this paper.

Acknowledgements We acknowledge discussions with J. Checkelsky, S. Chen, C. Dean, M. Yankowitz, D. Reilly, I. Sodemann and M. Zaletel. Work at UCSB was primarily supported by the ARO under MURI W911NF-16-1-0361. Measurements of twisted bilayer graphene (Extended Data Fig. 8) and measurements at elevated temperatures (Extended Data Fig. 3) were supported by a SEED grant and made use of shared facilities of the UCSB MRSEC (NSF DMR 1720256), a member of the Materials Research Facilities Network (www.mrfn.org). A.F.Y. acknowledges the support of the David and Lucille Packard Foundation under award 2016-65145. A.H.M. and J.Z. were supported by the National Science Foundation through the Center for Dynamics and Control of Materials, an NSF MRSEC under Cooperative Agreement number DMR-1720595, and by the Welch Foundation under grant TBF1473. C.L.T. acknowledges support from the Hertz Foundation and from the National Science Foundation Graduate Research Fellowship Program under grant 1650114. K.W. and T.T. acknowledge support from the Elemental Strategy Initiative conducted by the MEXT, Japan, Grant Number JPMXP0112101001, JSPS KAKENHI grant numbers JP20H00354 and the CREST(JPMJCR15F3), JST.

Author contributions H.P., M.A.K. and Y.Z. fabricated the devices. H.P., F.Y., C.L.T. and M.S. performed the measurements, advised by A.F.Y. J.Z. and A.H.M. performed the band structure calculations. K.W. and T.T. grew the hexagonal boron nitride crystals. H.P., A.H.M. and A.F.Y. wrote the manuscript with input from all other authors.

Competing interests The authors declare no competing interests.

Additional information
Supplementary information is available for this paper at https://doi.org/10.1038/s41586-020-2963-8.
Correspondence and requests for materials should be addressed to A.F.Y.
Peer review information *Nature* thanks the anonymous reviewers for their contribution to the peer review of this work. Peer reviewer reports are available.
Reprints and permissions information is available at http://www.nature.com/reprints.

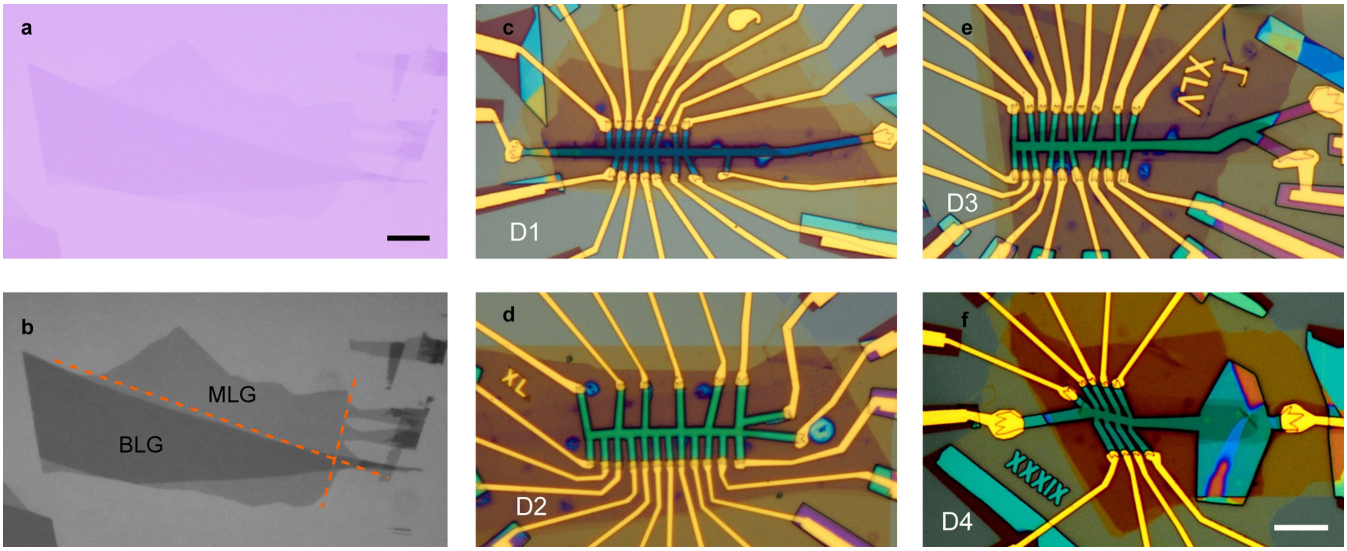

Extended Data Fig. 1 | tMBG devices. a, Optical image of a typical graphene flake containing both MLG and BLG domains. **b**, The same image as in **a** but in greyscale and with enhanced contrast to clearly show the graphene flake. Dashed lines show the lines along which the flake was cut using atomic force microscopy. **c**–**f**, Optical images of completed tMBG devices D1 (**c**), D2 (**d**), D3 (**e**) and D4 (**f**). All scale bars, 10 µm.

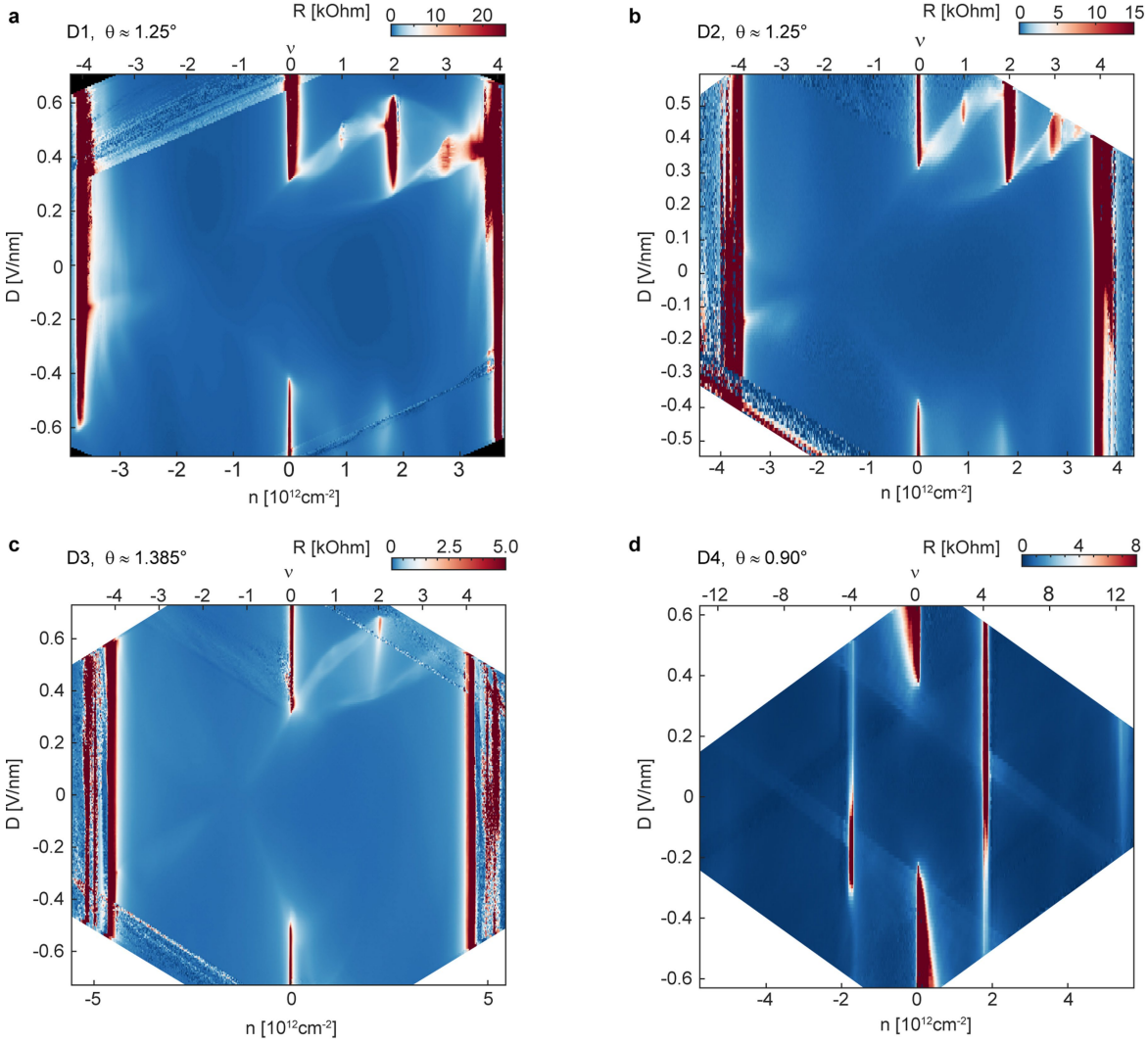

Extended Data Fig. 2 | Longitudinal resistance of tMBG devices with different twist angles. a–**d**, Longitudinal resistance R_{xx} of devices D1 with $\theta \approx 1.25(1)°$ (**a**), D2 with $\theta \approx 1.25(1)°$ (**b**), D3 with $\theta = 1.385(5)°$ (**c**) and D4 with $\theta \approx 0.90(1)°$ (**d**). The numbers in parentheses indicate the uncertainty in the final digit. All measurements are performed at zero magnetic field and $T \approx 20$ mK.

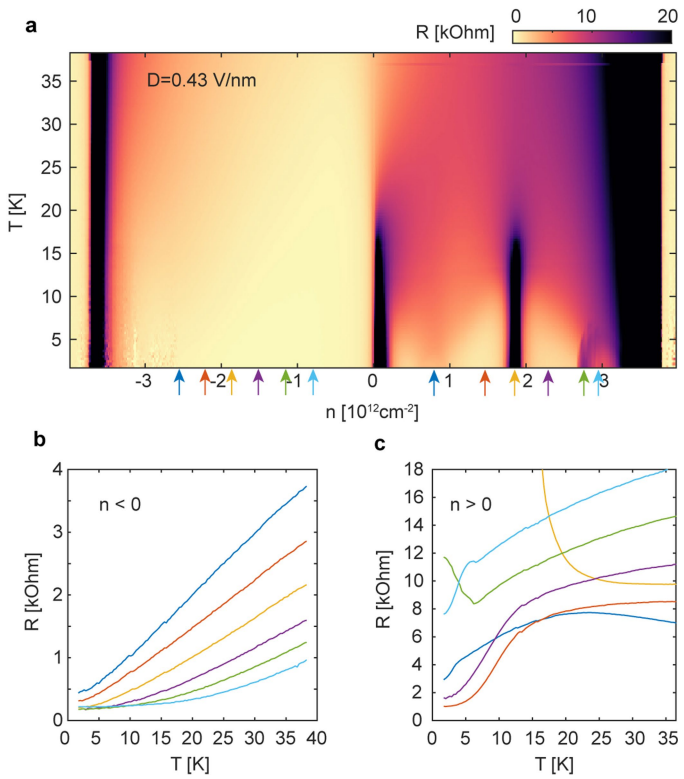

Extended Data Fig. 3 | Temperature dependence of the correlated states in device D1. a, Temperature-dependent resistance measured at $D = 0.43\ \mathrm{V\,nm^{-1}}$ in device D1. **b**, **c**, Temperature-dependent resistance at selected carrier densities, marked by the arrows in **a**, for $n < 0$ (**b**) and $n > 0$ (**c**).

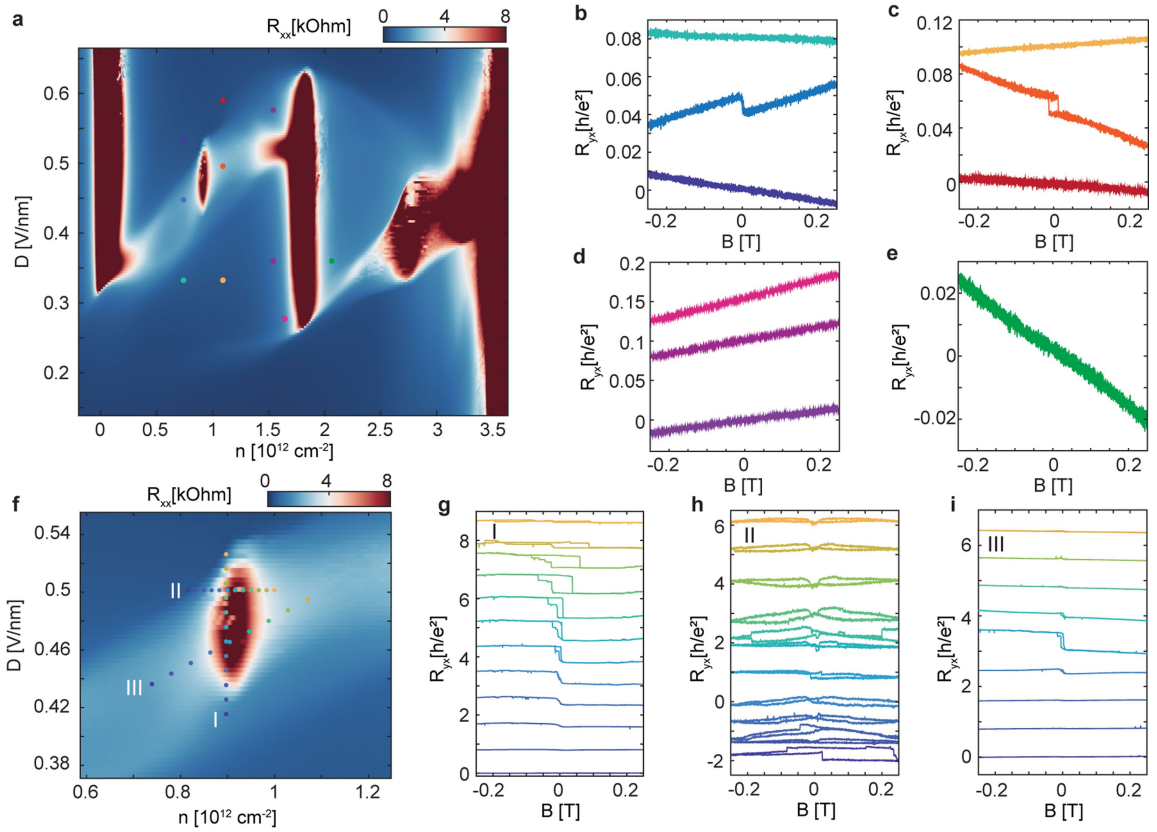

Extended Data Fig. 4 | Development of Hall resistance at different *n* and *D* in device D1. a, Longitudinal resistance R_{xx} of the correlated region at $B = 0$ T. **b**–**e**, Hall resistance R_{yx} measured at *n* and *D* marked by the dots in **a**. The colour of the dots in **a** corresponds to the colour of curves in **b**–**e**. Panels **b** and **c** show curves taken at small negative and positive dopings of $\nu = 1$. Panels **d** and **e** show curves taken at small negative and positive dopings of $\nu = 2$. **f**, Zoom-in of R_{xx} around $\nu = 1$. **g**–**i**, R_{yx} measured along the line cuts I (**g**), II (**h**) and III (**i**). R_{yx} in the plots are shifted by an offset.

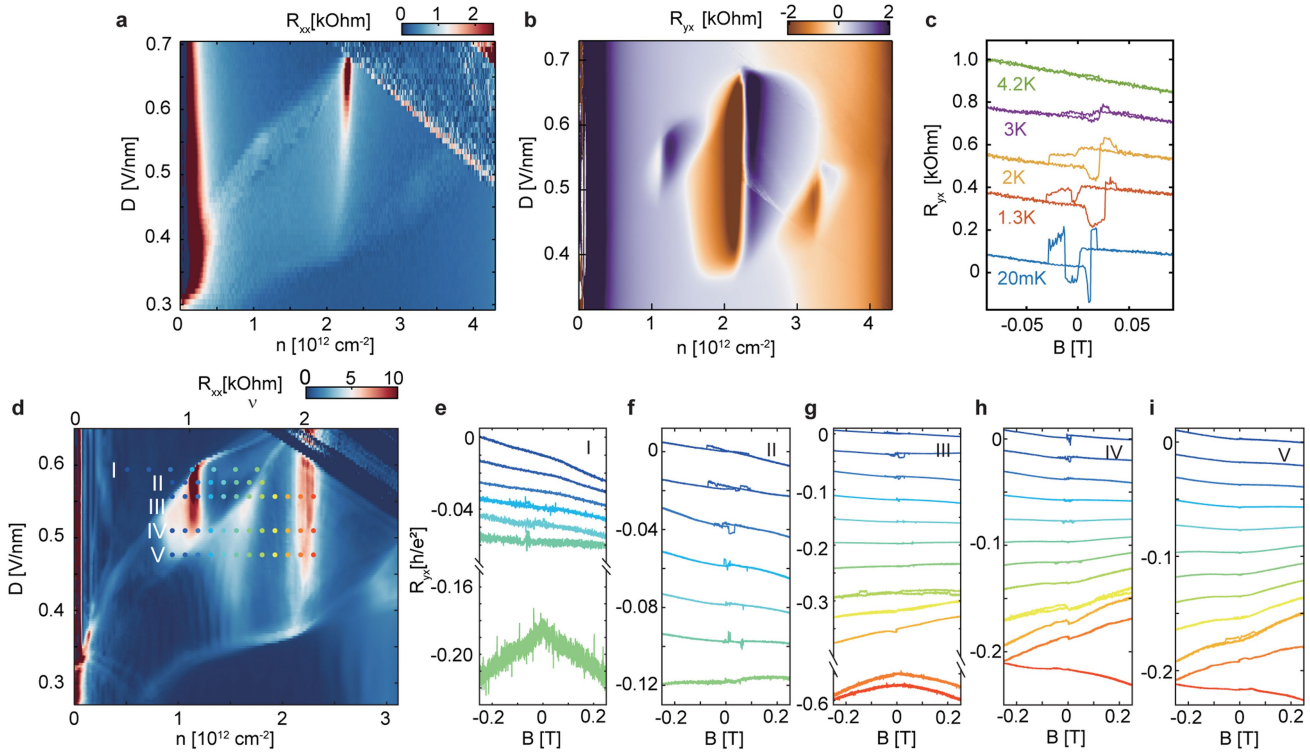

Extended Data Fig. 5 | Development of Hall resistance in device D3. **a**, Longitudinal resistance R_{xx} of the correlated region at $B = 0$ T. **b**, Hall resistance R_{yx} of the same region as in **a**. **c**, Temperature dependence of R_{yx} at $\nu = 1$. The anomalous Hall effect disappears at 4.2 K. **d**, R_{xx} of the correlated region measured at $B = 2$ T. **e**–**i**, R_{yx} along the line cuts I (**e**), II (**f**), III (**g**), IV (**h**) and V (**i**).

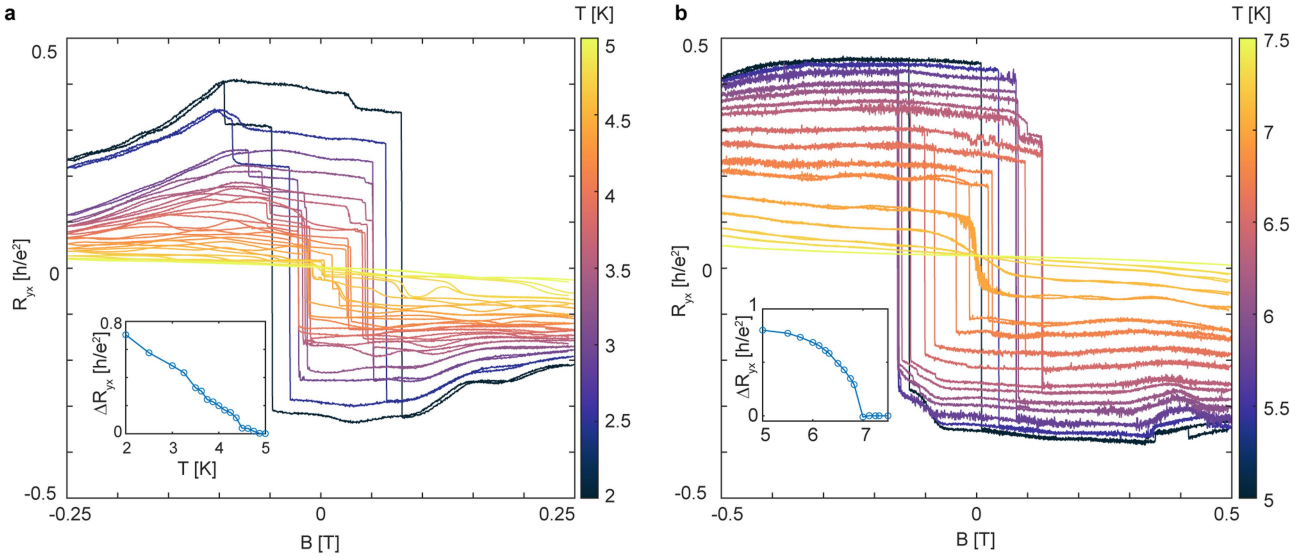

Extended Data Fig. 6 | Temperature dependence of the hysteresis at $\nu = 1$ and $\nu = 3$ in device D1. a, **b**, Temperature dependence of the Hall resistance R_{yx} measured at $\nu = 1$ (**a**) and $\nu = 3$ (**b**). Insets show the temperature dependence of the height of the hysteresis loop height, as defined in Fig. 3a.

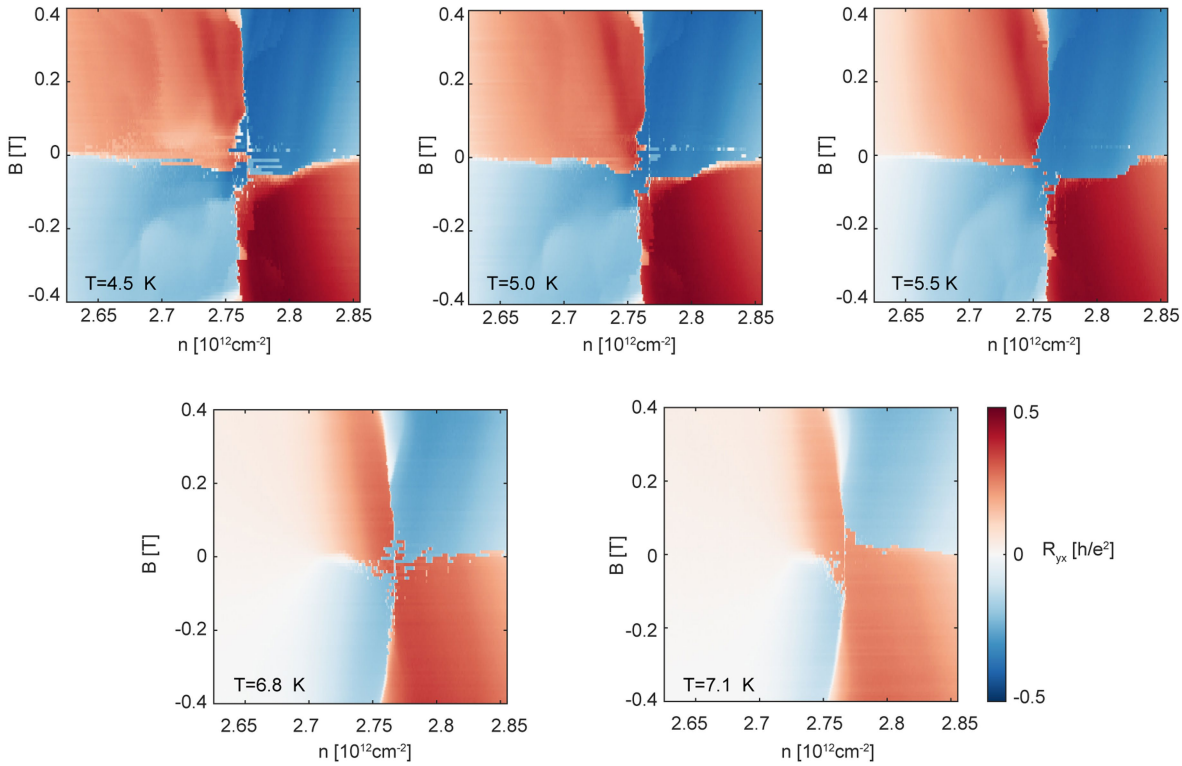

Extended Data Fig. 7 | *n* and *B* dependence of the measured anomalous Hall effect, plotted at selected temperatures for $D = 0.4\ \mathrm{V\,nm^{-1}}$ in device D1. Temperatures are labelled on the individual panels.

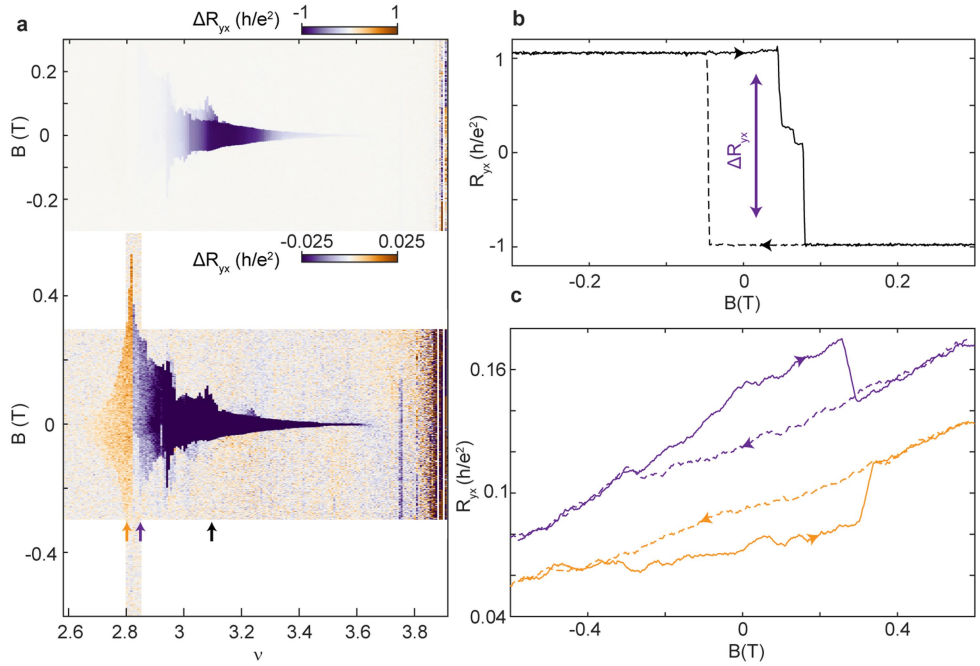

Extended Data Fig. 8 | Magnetization reversal in tBLG. a, Anomalous Hall resistance ΔR_{yx} associated with tBLG ferromagnetism, extracted by subtracting $R_{yx}(B)$ as B is increased from $R_{yx}(B)$ as B is decreased. The tBLG device is the same as in ref. [4]. The colour scale is fixed to the von Klitzing constant in the top of the plot to show the range of filling factors for which a robust quantum anomalous Hall effect is observed. The colour scale axis is dramatically reduced in the bottom plot to illustrate weak features in $\Delta R_{yx}(\nu)$. For $\nu < 3$, the coercive field of the ferromagnetic order increases dramatically, peaking at $\nu = 2.82$ electrons per moiré unit cell. For $\nu < 2.82$, ΔR_{yx} switches sign, indicating that the valley polarization of the ground state of the system at finite magnetic field has switched. **b**, A robust $C = 1$ quantum anomalous Hall effect at $\nu = 3.1$. **c**, Ferromagnetic hysteresis plots on opposite sides of the divergence of the coercive field close to $\nu = 2.82$ (with offset). Note the change in the relative sign of ΔR_{yx}.

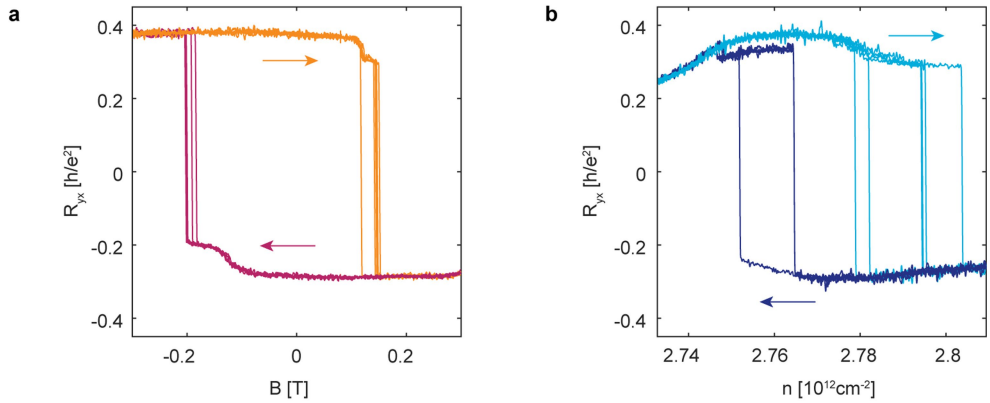

Extended Data Fig. 9 | Repeatability of magnetization switching with *B* and *n* measured in device D1. a, Repeated magnetic-field hysteresis loops. **b**, Repeated doping hysteresis loops. Both panels taken under conditions analogous to those in Fig. 4b, described in the main text.